

Quantum orbits in atomic ionization beyond the dipole approximation

A. S. Jašarević¹, D. Habibović¹, and D. B. Milošević^{1,2}

¹*University of Sarajevo, Faculty of Science, Zmaja od Bosne 35, 71000 Sarajevo, Bosnia and Herzegovina*

²*Academy of Sciences and Arts of Bosnia and Herzegovina, Bistrik 7, 71000 Sarajevo, Bosnia and Herzegovina*



(Received 14 June 2024; accepted 2 August 2024; published 26 August 2024)

Using the strong-field-approximation theory beyond the dipole approximation we investigate above-threshold ionization induced by the monochromatic and bichromatic laser fields. Particular emphasis is on the approach based on the saddle-point method and the quantum-orbit theory which provides an intuitive picture of the underlying process. In particular, we investigate how the solutions of the saddle-point equations and the corresponding quantum orbits and velocities are affected by the nondipole effects. The photoelectron trajectories are two dimensional for linearly polarized field and three dimensional for two-component tailored fields, and the electron motion in the propagation direction appears due to the nondipole corrections. We show that the influence of these corrections is not the same for all contributions of different saddle-point solutions. For a linearly polarized driving field, we focus our attention only on the rescattered electrons. On the other hand, for the tailored driving field, exemplified by the $\omega-2\omega$ orthogonally polarized two-color field, which is of the current interest in the strong-field community, we devote our attention to both the direct and the rescattered electrons. In this case, we quantitatively investigate the shift which appears in the photoelectron momentum distribution due to the nondipole effects and explain how these corrections affect the quantum orbits and velocities which correspond to the saddle-point solutions.

DOI: [10.1103/PhysRevA.110.023111](https://doi.org/10.1103/PhysRevA.110.023111)

I. INTRODUCTION

To investigate atomic processes induced by the strong laser fields the dipole approximation is typically employed. This approximation assumes that the relation between the vector potential $\mathbf{A}(t)$ and the corresponding electric field $\mathbf{E}(t)$ is given by $\mathbf{A}(t) = -\int^t dt' \mathbf{E}(t')$ so that the magnetic field $\mathbf{B} = \nabla \times \mathbf{A}(t)$ vanishes. The parameters of the Ti:sapphire laser (the intensity of the order of 10^{14} W/cm² and the wavelength around 800 nm), which was employed extensively to induce strong-field processes, are such that the application of the dipole approximation is justified. However, as the laser systems with higher intensity [1,2] and/or longer wavelengths [3,4] than the Ti:sapphire laser became available, the use of the dipole approximation became questionable. If the dipole approximation breaks down, the alternative approach is based on the fully relativistic treatment. However, for the laser-field parameters which are such that the dipole approximation is not justified but the fully relativistic treatment is still not necessary, it is enough to take into account the nondipole corrections. These corrections are of the order of $1/c$, where c is the speed of light, while the relativistic corrections are of the order of $1/c^2$. For a linearly polarized laser field, two parameters were introduced to help assessing which corrections on the dipole approximation are necessary. These parameters

are defined by [3,5]

$$z_f = \frac{2U_p}{mc^2}, \quad \beta_0 \approx \frac{U_p}{2mc\omega}, \quad (1)$$

with U_p being the ponderomotive energy, while m and ω are the electron mass and the driving-field frequency, respectively. If $z_f \ll 1$, i.e., if $2U_p$ is much lower than the rest energy of the electron, the relativistic corrections are not necessary. On the other hand, the parameter β_0 represents the amplitude of the electrons' motion in the propagation direction. If $\beta_0 \gtrsim 1$ a.u., the nondipole corrections are necessary. The influence of the nondipole effects on the strong-field processes has been observed in Refs. [4,6–10] (see also the review papers [11–13]).

In recent years, nondipole effects have been investigated by many groups. For example, the nondipole corrections were analyzed in Refs. [9,10,14–18] both experimentally and theoretically. In addition, the nondipole Hamiltonian was investigated in Ref. [19], while the nondipole effects for the laser-assisted electron scattering and for the strong-field ionization were scrutinized in Refs. [20–22], respectively. Also, the nondipole corrections for the high-order harmonic generation were analyzed in Refs. [23,24], while the relativistic theory was considered in Refs. [25–28]. The approach which enables one to investigate the nondipole corrections together with the influence of the structured-light fields was utilized in Ref. [29]. Finally, the corrections on the dipole approximation were also investigated in Refs. [30–33] with particular emphasis on the ultrashort linearly and circularly polarized pulses.

Besides the fact that the most accurate data are obtained using the *ab initio* theories, the involved calculations are

Published by the American Physical Society under the terms of the [Creative Commons Attribution 4.0 International license](https://creativecommons.org/licenses/by/4.0/). Further distribution of this work must maintain attribution to the author(s) and the published article's title, journal citation, and DOI.

usually time consuming even for simple atomic systems. For this reason, many semi-analytical theories have been developed [34]. Among those, particularly successful are the theories based on the strong-field approximation (SFA) which neglects the interaction of the freed electron with the parent core after the ionization. Our SFA theory is based on the single-active-electron approximation. Multielectron effects are included via modeling of the ground-state wave functions using the Roothaan-Hartree-Fock method and an expansion in Slater-type orbitals, and using an effective rescattering potential. The dynamical multielectron effects and electronic correlations are neglected (in Refs. [35,36] it was shown that such corrections are restricted to the low-energy part of the spectrum which is not of our interest here). Our SFA theory allows accurate modeling of the high-order above-threshold ionization (HATI) process [37]. In this process, after the electron is released from the atom by an intense laser field, it propagates in the continuum and either reaches the detector directly [in which case the process is denoted as above-threshold ionization (ATI)] or undergoes rescattering at the parent core. The influence of the neglected Coulomb potential is small, particularly in the laser-field-parameters regimes in which nondipole effects become significant [38] [see Figs. 10(c) and 10(d) in Ref. [38]]. The Coulomb effects are significant only in the low-energy region and for the driving field with wavelength and intensity for which the nondipole effects are negligible.

Recently, our SFA-based theory was modified to incorporate the nondipole corrections [39,40]. In addition, we have generalized the obtained theory to the case of the tailored laser fields [41]. These fields have attracted significant attention due to the large number of parameters which can be used to control the process. Surprisingly, the nondipole corrections for the tailored driving fields have received almost no attention at all. A particularly important example of tailored laser fields is the orthogonally polarized two-color field (OTC), which consists of two linearly polarized components with mutually orthogonal polarizations. The electron tunneling induced by an OTC field was analyzed in Ref. [42] for negative ions and in Refs. [43–58] for atoms. Furthermore, the temporal double-slit experiment [59] with an OTC field was realized in Ref. [60], while the control of the electron spin polarization in strong-field ionization [61] using the OTC field was proposed in Ref. [62]. Moreover, this field configuration allows the generation of elliptically polarized high-order harmonics [63–65] with ellipticity which can be controlled using the field parameters. Finally, it has been shown that an OTC field can be successfully utilized to study chirality (see Ref. [66] and references therein). In conclusion, it is clear that the OTC tailored field has recently attracted a lot of interests in the strong-field community. Therefore, we decided to use this field to illustrate our theory.

The physical insight into the explored process can be acquired by using the saddle-point (SP) method [67,68]. This allows one to introduce the idea of the quantum orbits and relate them with the electron trajectories in the laser field. In the present paper, we investigate the influence of the nondipole corrections on the quantum orbits which correspond to different solutions of the SP equations for both the linearly polarized and the tailored driving fields. In addition, we

investigate how these corrections affect the partial contributions of the SP solutions to the photoelectron yield as well as the total photoelectron spectrum.

The paper is organized as follows: In Sec. II we briefly recapitulate our nondipole SFA-based theory and discuss the saddle-point method. Also, we introduce the quantum orbits and relate them to the electron trajectories. In Sec. III we present our numerical results for the linearly polarized field as well as for the OTC field which we use as an example of the tailored field. Finally, in Sec. IV we state our main conclusions. Atomic units are used unless otherwise stated.

II. THEORY

A. Differential ionization rate

For the T -periodic laser field, the differential ionization rate for the emission of the photoelectron with momentum \mathbf{p} and energy $E_{\mathbf{p}} = \mathbf{p}^2/2$ is

$$w_{\mathbf{p}i}(n) = 2\pi p |T_{\mathbf{p}i}(n)|^2, \quad (2)$$

where n is the number of absorbed photons and $T_{\mathbf{p}i}(n)$ is the T -matrix element. Within the strong-field approximation, after the ionization, the continuum is approximated by the field-dressed plane waves and the eventual rescattering events are incorporated via a Born-type series expansion [69–72]. The zeroth-order contribution to the T -matrix element is [39,40]

$$T_{\mathbf{p}i}^{(0)}(n) = \int_0^T \frac{dt_0}{T} \langle \mathbf{q}_{\mathbf{p}}(t_0) | H_{\text{int}}(t_0) | \psi_i \rangle e^{iS(\mathbf{p};t_0)}, \quad (3)$$

and it corresponds to the so-called direct electrons, i.e., the electrons which do not interact with the parent ion after liberation. The nondipole effects are included by expanding the vector potential as

$$\mathbf{A}(\xi) \approx \mathbf{A}(t) + \frac{\hat{\mathbf{k}} \cdot \mathbf{r}}{c} \mathbf{E}(t), \quad (4)$$

with $\xi = t - \hat{\mathbf{k}} \cdot \mathbf{r}/c$, which consequently leads to the interaction Hamiltonian of the form [73]

$$H_{\text{int}}(t) = \mathbf{E}(t) \cdot \left(\mathbf{r} - i \frac{\hat{\mathbf{k}} \cdot \mathbf{r}}{c} \nabla \right), \quad (5)$$

with c being the speed of light. The first term corresponds to the dipole approximation, while the second term couples the coordinate in the field propagation direction (determined by the unit vector $\hat{\mathbf{k}} = \hat{\mathbf{e}}_z$) to the components of momentum in the polarization plane. The solutions of the Schrödinger equation for this Hamiltonian are the nondipole Volkov states [73] $|\chi_{\mathbf{p}}(t)\rangle = |\mathbf{q}_{\mathbf{p}}(t)\rangle e^{-iS_{\mathbf{p}}(t)}$ with $S_{\mathbf{p}}(t) = \frac{1}{2} \int^t dt' \mathbf{q}_{\mathbf{p}}^2(t')$ and

$$\mathbf{q}_{\mathbf{p}}(t) = \mathbf{p} + \mathbf{A}(t) + \hat{\mathbf{k}}[\mathbf{p} \cdot \mathbf{A}(t) + \mathbf{A}^2(t)/2]/c. \quad (6)$$

Also, the action of the direct electrons is $S(\mathbf{p};t_0) = S_{\mathbf{p}}(t_0) + I_p t_0$, with I_p the ionization potential, and $\psi_i \equiv \psi_{ilm}(\mathbf{r}) = R_{il}(r) Y_{lm}(\theta, \phi)$ the initial ground state where $Y_{lm}(\theta, \phi)$ are normalized spherical harmonics, while the radial functions $R_{il}(r)$ can be represented either as a linear combination of the Slater-type orbitals [74–77] or by the asymptotic wave functions [37,77,78]. The explicit form of the radial wave

function in both cases can be found in Ref. [40]. The Slater-type wave functions take into account all electrons of the atom but neglect the electron dynamics.

The next term of the Born-type-series expansion corresponds to the rescattered electrons and the contribution to the T -matrix element is [39,40]

$$T_{\mathbf{p}i}^{(1)}(n) = -i \int_0^T \frac{dt}{T} \int_{-\infty}^t dt_0 \left[\frac{2\pi}{i(t-t_0)} \right]^{3/2} e^{iS_{\mathbf{p},st}(t_0,t)} \times \langle \mathbf{p} + \mathbf{p} \cdot \mathbf{A}(t) \hat{\mathbf{k}}/c | V(\mathbf{r}) | \mathbf{K}_{st} + \mathbf{K}_{st} \cdot \mathbf{A}(t) \hat{\mathbf{k}}/c \rangle \times \langle \mathbf{q}_{\mathbf{K}_{st}}(t_0) | H_{\text{int}}(t_0) | \psi_i \rangle. \quad (7)$$

Here, $\mathbf{K}_{st}(t_0, t) = \mathbf{k}_{st}(t_0, t) + \kappa(t_0, t) \hat{\mathbf{k}}/c$ with $\mathbf{k}_{st}(t_0, t) = -\int_{t_0}^t dt' \mathbf{A}(t')/(t-t_0)$ being the stationary momentum and $\kappa(t_0, t) = \mathbf{k}_{st}^2(t_0, t) - [\mathcal{U}_1(t) - \mathcal{U}_1(t_0)]/(t-t_0) - U_p$, where $\int^t dt' \mathbf{A}^2(t')/2 = U_p t + \mathcal{U}_1(t)$ and U_p is the ponderomotive energy. The action of the rescattered electrons is

$$S_{\mathbf{p},st}(t_0, t) = S_{\mathbf{p}}(t) - \frac{1}{2} \int_{t_0}^t dt' \mathbf{q}_{\mathbf{K}_{st}}^2(t') + I_p t_0, \quad (8)$$

where t_0 and t are the ionization and rescattering times, respectively. Finally, we model our rescattering potential $V(\mathbf{r})$ by the double Yukawa potential [79].

Our driving field consists of two linearly polarized components with mutually orthogonal polarizations

$$\mathbf{E}(t) = E_1 \sin(r\omega t) \hat{\mathbf{e}}_x + E_2 \sin(s\omega t + \varphi) \hat{\mathbf{e}}_y, \quad (9)$$

where E_j , $j = 1, 2$, are the electric-field amplitudes, ω is the fundamental frequency, and φ is the relative phase. Also, r and s are integers, i.e., the frequencies of the field components are integer multiples of the fundamental frequency ω and $\hat{\mathbf{e}}_x$ and $\hat{\mathbf{e}}_y$ define the laser-field polarization plane. For $E_2 = 0$ the field becomes a linearly polarized monochromatic field. Otherwise, the driving field is the orthogonally polarized two-color field.

B. Saddle-point method

The integrals which appear in Eqs. (3) and (7) can be solved either numerically or by using the saddle-point method. In the latter case, the condition that the action of the direct electrons is stationary $dS(\mathbf{p}; t_0)/dt_0 = 0$ leads to the equation $\mathbf{q}_{\mathbf{p}}^2(t_0) = -2I_p$ which represents the energy-conservation condition at the ionization time. Because the nondipole effects are of the order of $1/c$, the term proportional to $1/c^2$, which appears when we introduce $\mathbf{q}_{\mathbf{p}}$ in the direct SP equation, should be neglected. For the initial state represented by the asymptotic wave function, the contribution of the direct electrons to the T -matrix element is [78,80]

$$T_{\mathbf{p}i}^{(0),SP}(n) = i2^{-3/2} T^{-1} A \kappa_0^{\nu} \nu \Gamma(\nu/2) \times \sum_{t_{0s}} \left(\frac{q_s}{i\kappa_0} \right)^l Y_{lm}(\hat{\mathbf{q}}_{\mathbf{p}s}) e^{iS_s} \left(\frac{2i}{S_s''} \right)^{(\nu+1)/2}, \quad (10)$$

where the summation is over the solutions t_{0s} of the SP equation located in the upper half of the complex plane,

$\mathbf{q}_{\mathbf{p}s} \equiv \mathbf{q}_{\mathbf{p}}(t_{0s})$, $S_s \equiv S(\mathbf{p}; t_{0s})$, and

$$S_s'' \equiv \frac{d^2 S(\mathbf{p}; t_{0s})}{dt_0^2} = -\mathbf{q}_{\mathbf{p}}(t_{0s}) \cdot \{ \mathbf{E}(t_{0s}) + \mathbf{E}(t_{0s}) \cdot [\mathbf{p} + \mathbf{A}(t_{0s})] \hat{\mathbf{k}}/c \}. \quad (11)$$

The number of solutions of the SP equation for the direct electrons can be determined following the procedure elaborated in Ref. [81]. The easiest way to classify these solutions is by introducing the index η so that the increase in the value of this index is related to the increase of the real part of the ionization time.

On the other hand, the stationarity conditions for the rescattering action are $\partial S_{\mathbf{p},st}(t_0, t)/\partial t_0 = 0$ and $\partial S_{\mathbf{p},st}(t_0, t)/\partial t = 0$ and they lead to the SP equations $\mathbf{q}_{\mathbf{K}_{st}}^2(t_0) = -2I_p$ and $\mathbf{q}_{\mathbf{K}_{st}}^2(t) = \mathbf{q}_{\mathbf{p}}^2(t)$. These equations represent the energy-conservation conditions at the ionization and rescattering times, respectively. To obtain only nondipole corrections, the terms proportional to $1/c^2$ should be discarded. The SP method, presented in Ref. [80], leads to the following expression for the rescattering T -matrix element

$$T_{\mathbf{p}i}^{(1),SP}(n) = \pi^2 T^{-1} A \kappa_0^{\nu} \nu \Gamma(\nu/2) \sum_{\{t_{0s}, t_s\}} \left(\frac{q_{\mathbf{K}_{st,s}}}{i\kappa_0} \right)^l e^{iS_{st,s}} \times Y_{lm}(\hat{\mathbf{q}}_{\mathbf{K}_{st,s}}) \frac{\langle \mathbf{p} | V | \mathbf{k}_{st} \rangle}{[i(t_s - t_{0s})]^{3/2}} \times \left(\frac{2i}{S_{st0,s}''} \right)^{(\nu+1)/2} \left(\frac{2i}{S_{st,s}''} \right)^{1/2}, \quad (12)$$

where $\mathbf{q}_{\mathbf{K}_{st,s}} \equiv \mathbf{q}_{\mathbf{K}_{st}}(t_{0s})$, $S_{st,s} \equiv S_{\mathbf{p},st}(t_{0s}, t_s)$, $S_{st0,s}'' \equiv \partial^2 S_{\mathbf{p},st}(t_0, t)/\partial t_0^2|_{t_{0s}, t_s}$, and $S_{st,s}'' \equiv \partial^2 S_{\mathbf{p},st}(t_0, t)/\partial t^2|_{t_{0s}, t_s}$. The high-energy solutions of the HATI SP equations appear in pairs and they can be classified using the multi-index (α, β, m) . In particular, for a fixed value of the rescattering time $0 \leq t < T$, the values of the ionization time t_0 are ordered using the index $m = 0, 1, \dots$ in such a way that m represents the approximate value of the travel time $\tau = t - t_0$ in units of the laser period. Furthermore, the index β counts different pairs of solutions with the same m , while the index α distinguishes different solutions of a given pair. This classification was introduced for the bicircular field in Ref. [80], but it can also be applied to an arbitrary driving field [68]. For a linearly polarized monochromatic field it was introduced in Refs. [82,83].

C. Quantum orbits

The nondipole correction $(\hat{\mathbf{k}} \cdot \mathbf{r})\mathbf{E}(t)/c$ in vector potential (4) leads to the magnetic field

$$\mathbf{B}(\xi) = \nabla \times \mathbf{A}(\xi) \approx -\frac{1}{c} [E_y(t) \hat{\mathbf{e}}_x - E_x(t) \hat{\mathbf{e}}_y]. \quad (13)$$

The corresponding equations of motion are given by

$$\ddot{\mathbf{r}}(t) = -\mathbf{E}(\xi) - \dot{\mathbf{r}}(t) \times \mathbf{B}(\xi). \quad (14)$$

By expanding the electric field $\mathbf{E}(\xi)$ as

$$\mathbf{E}(\xi) \approx \mathbf{E}(t) - \frac{\hat{\mathbf{k}} \cdot \mathbf{r}}{c} \dot{\mathbf{E}}(t), \quad (15)$$

and using $\mathbf{r}(t) \approx \mathbf{r}_0(t) + \mathbf{r}_c(t)$, where $\mathbf{r}_c(t)$ is the nondipole correction of the order $1/c$, we obtain the equations

$$\ddot{\mathbf{r}}_0(t) = -\mathbf{E}(t), \quad \ddot{\mathbf{r}}_c(t) = -[\dot{\mathbf{r}}_0(t) \cdot \mathbf{E}(t)]\hat{\mathbf{k}}/c. \quad (16)$$

The equation for $\mathbf{r}_0(t)$ is the equation of motion in the dipole approximation, with the solution

$$\mathbf{r}_0(t') = \begin{cases} (t' - t_0)\mathbf{k}_{\text{st}} + \boldsymbol{\alpha}(t') - \boldsymbol{\alpha}(t_0), & t_0 \leq t' \leq t \\ (t' - t)\mathbf{p} + \boldsymbol{\alpha}(t') - \boldsymbol{\alpha}(t), & t' > t, \end{cases} \quad (17)$$

where $\boldsymbol{\alpha}(t) = \int^t \mathbf{A}(t')dt'$. The corresponding velocity is

$$\mathbf{v}_0(t') = \frac{d\mathbf{r}_0(t')}{dt'} = \begin{cases} \mathbf{k}_{\text{st}} + \mathbf{A}(t'), & t_0 \leq t' \leq t \\ \mathbf{p} + \mathbf{A}(t'), & t' > t. \end{cases} \quad (18)$$

The solution for $\mathbf{r}_c(t)$ is given by

$$\mathbf{r}_c(t) = \{\mathbf{k}_{\text{st}} \cdot [\boldsymbol{\alpha}(t') - \boldsymbol{\alpha}(t_0)] + \mathcal{U}_1(t') - \mathcal{U}_1(t_0) + [U_p + \kappa(t_0, t)](t' - t_0)\}\hat{\mathbf{k}}/c, \quad t_0 \leq t' \leq t, \quad (19)$$

and

$$\mathbf{r}_c(t) = \{\mathbf{p} \cdot [\boldsymbol{\alpha}(t') - \boldsymbol{\alpha}(t)] + \mathcal{U}_1(t') - \mathcal{U}_1(t) + U_p(t' - t)\}\hat{\mathbf{k}}/c, \quad t' > t. \quad (20)$$

The corresponding velocity $\mathbf{v}_c(t') = d\mathbf{r}_c(t')/dt'$ reads

$$\mathbf{v}_c(t') = \{\mathbf{k}_{\text{st}} \cdot \mathbf{A}(t') + \mathbf{A}^2(t')/2 + \kappa(t_0, t)\}\hat{\mathbf{k}}/c, \quad t_0 \leq t' \leq t, \quad (21)$$

and

$$\mathbf{v}_c(t') = \{\mathbf{p} \cdot \mathbf{A}(t') + \mathbf{A}^2(t')/2\}\hat{\mathbf{k}}/c, \quad t' > t. \quad (22)$$

The saddle-point solutions for the ionization and rescattering times are complex numbers. The quantum orbits and velocities are defined by the previously introduced solutions of the classical equation of motion but for the complex ionization and rescattering times. It is a common practice to present only the projection of the quantum orbits and velocities onto a real axis, for the real time $t' \geq \text{Re } t$.

III. NUMERICAL RESULTS

In this section, we present our numerical results using the example of the He atom which has the s ground state (the magnetic quantum number is $m = 0$) and the ionization potential $I_p = 24.59$ eV. For the He atom, the influence of the multielectron effects was investigated in Ref. [35] for the high-order harmonic generation process, and it was found that it is restricted to the low-energy part of the spectrum. Similar behavior is expected for the HATI process. First, we investigate the trajectories of the HATI photoelectrons liberated by the linearly polarized field by taking into account the nondipole corrections. Second, we analyze the similar process induced by the OTC driving field. Our coordinate system is defined by the unit vectors $\hat{\mathbf{e}}_x$, $\hat{\mathbf{e}}_y$, and $\hat{\mathbf{e}}_z$. The direction of the photoelectron emission is defined by the spherical angles θ and ϕ . The angle θ is the angle between the unit vector $\hat{\mathbf{e}}_z$ and the final photoelectron momentum \mathbf{p} , while the angle ϕ is the angle between the unit vector $\hat{\mathbf{e}}_x$ and the projection of the final photoelectron momentum on the xy plane.

A. Linearly polarized field

The influence of the nondipole effects on the direct electrons obtained using a linearly polarized monochromatic field was investigated in the previous publications [39,40]. In the present paper, we devote our attention to the rescattered electrons. In particular, we investigate the photoelectron trajectories for the HATI induced by the linearly polarized field with the intensity $I = E_1^2 = 10^{15}$ W/cm² and the wavelength of 2500 nm. For these values of the driving-field parameters, $\beta_0 = 4.2$ a.u., and the nondipole effects should not be neglected. Also, due to the high ionization potential, helium can withstand this field without immediate ionization so that the saturation effects can be neglected. In Fig. 1(a) we present the partial contributions to the differential ionization rate of different saddle-point solutions together with the coherent sum of these contributions (black dotted line, circles). The corresponding values of the multi-index (α, β, m) are indicated in the legend, and the contributions which should be discarded after the cutoff are presented by the dashed lines [82,83]. The results are obtained for the emission in the direction $\phi = 0^\circ$ and $\theta = 87^\circ$. The reason why we have chosen $\theta = 87^\circ$ instead of $\theta = 90^\circ$ lies in the fact that, due to the nondipole effects, the photoelectron spectrum will be the longest around this direction (see, for example, Fig. 4 in Ref. [40]). For the photoelectron energy $E_p > 7U_p$, the contributions of the pair of solutions with $(\beta, m) = (1, 0)$ [red lines in Fig. 1(a)] are dominant except for the narrow region around $7.5U_p$ ($8.9U_p$) where the contributions of the solutions with $(\beta, m) = (2, 1)$ [$(\beta, m) = (1, 1)$] are also relevant. On the other hand, the photoelectron spectrum for $E_p < 7U_p$ is dominated by the solutions with $(\beta, m) = (2, 0)$ [green lines in Fig. 1(a)] and the solution with $(\alpha, \beta, m) = (-1, 1, 0)$ [red solid line in Fig. 1(a)]. Finally, for $E_p < 2U_p$, the solution with $(\alpha, \beta, m) = (-1, 0, 0)$ [maroon solid line in Fig. 1(a)] is the most significant. However, in this part of the photoelectron spectrum, the contributions of the direct electrons (not shown in Fig. 1) are most prominent. Figure 1(b) displays the comparison of the photoelectron spectra calculated using the SP method (black dotted line, circles) and by the numerical integration (brown solid line). The agreement between the obtained result is excellent proving that the SP method can be used to accurately calculate the photoelectron spectrum.

Once the requisite SP solutions are obtained, enabling the successful reproduction of the photoelectron spectra calculated by numerical integration, our attention is directed towards the quantum orbits and velocities associated with these solutions. In Fig. 2 we present the quantum orbits and corresponding velocities for the dominant pair of solutions [$(\beta, m) = (1, 0)$] in the high-energy part of the spectrum for the photoelectron energies $8U_p$, $9U_p$, and $10U_p$. The quantum orbits of the two solutions in this pair have the same shape, but the solution with $\alpha = -1$ (lower panels) has a slightly longer orbit than the solution with $\alpha = 1$ (upper panels) because it spends a slightly longer time in the laser field before rescattering occurs. It can also be seen that, for the solution $(\alpha, \beta, m) = (1, 1, 0)$ the orbits get longer as the photoelectron energy increases, whereas for the solution $(\alpha, \beta, m) = (-1, 1, 0)$, the orbits get shorter as the photoelectron energy

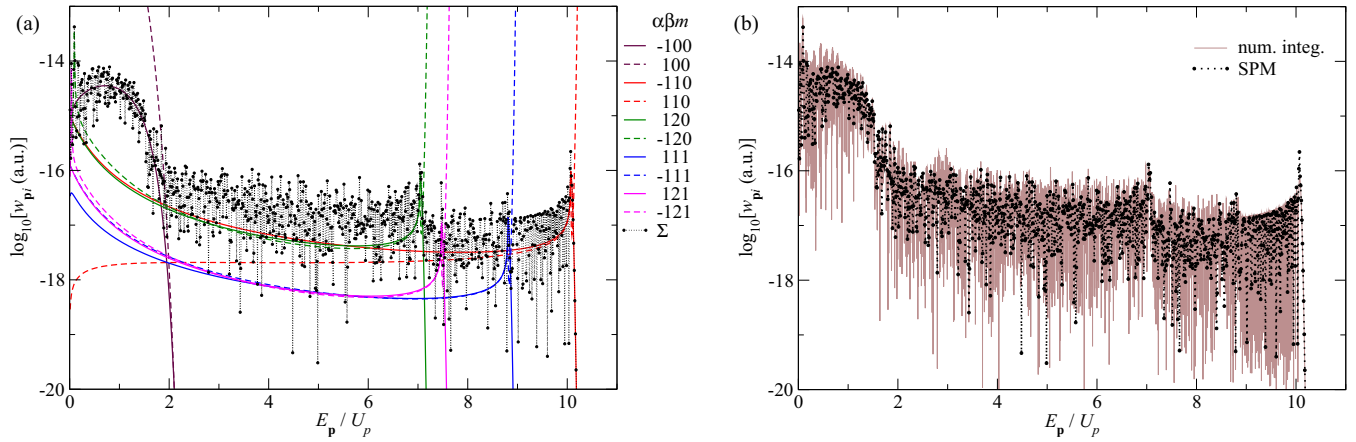


FIG. 1. (a) Partial contributions to the differential ionization rate of different saddle-point solutions together with the coherent sum of these contributions (black dotted line, circles) for HATI induced by exposing the He atom to the linearly polarized monochromatic field with intensity $I = E_1^2 = 10^{15}$ W/cm² and wavelength 2500 nm in the direction $\phi = 0^\circ$ and $\theta = 87^\circ$. The results are obtained using the theory which includes the nondipole corrections. (b) Comparison of the photoelectron spectra calculated using the SP method (black dotted line, circles) and by the numerical integration (brown solid line). Only rescattered electrons are taken into consideration.

increases. This can be explained by the fact that the two solutions merge at the cutoff energy, in the sense that the travel time of the solution with $\alpha = 1$ increases, while the travel time of the solution with $\alpha = -1$ decreases. We also note that, for both of these solutions, the electron moves only in the $x \geq 0$ part of the xz plane.

Now we investigate the trajectories in more detail. For example, we thoroughly examine the photoelectron trajectory and velocity for the solution $(\alpha, \beta, m) = (-1, 1, 0)$ and for

the photoelectron energy $E_p = 10U_p$ (black solid line in the lower left panel of Fig. 2). The photoelectron is born at the time $\text{Re } t_{0s} = -0.213T$ very close to the origin, with v_x component of velocity approximately equal to zero, and a small negative v_z component of velocity (the ionization velocity is indicated by the letter “I” in the lower-right panel of Fig. 2). The x component of the electron trajectory is determined only by the electric field and is governed by the equation $\ddot{x}(t) = -E_x(t)$, while in the z direction the electron is influenced by the magnetic field $B_y(t) = E_x(t)/c$ that is coupled with the v_x component of electron’s velocity, giving the equation $\ddot{z}(t) = -v_x(t)E_x(t)/c$ [see Eq. (16)]. At the ionization time, the electric field E_x is negative, and therefore the electron accelerates in the positive x direction. The positive velocity component v_x and negative electric field E_x imply acceleration in the positive z direction, causing the v_z component to become less and less negative. At the time $t = 0$, indicated by the violet circles denoted by “1” in the lower panels of Fig. 2, the direction of the electric field changes, and the electron starts to decelerate in the x direction. Since the v_x component is still positive and the electric field became positive as well, the electron starts to accelerate in the negative z direction. At the time $t = 0.212T$, indicated by the violet circle denoted by “2,” the electron’s v_x component of velocity becomes zero again, and now the electron starts to move in the negative x direction, while the v_z component of velocity decelerates its negative value. The v_z becomes positive at time $t = 0.323T$, indicated by the violet circles denoted by “3” and accelerates back to the parent ion where it rescatters at time $\text{Re } t_s = 0.491T$ (the rescattering velocity is indicated by the letter “R” in the lower-right panel of Fig. 2). After analyzing the high-energy part, we now turn our attention to the medium-energy part of the photoelectron spectrum. In Fig. 3 we presented the photoelectron trajectories and corresponding velocities for the SP solution $(\alpha, \beta, m) = (1, 2, 0)$ for photoelectron energies $3U_p, 5U_p,$ and $7U_p$. The contribution of this solution is the most significant [together with the solution with $(\alpha, \beta, m) = (-1, 1, 0)$] in the medium-energy part of the spectrum. Similarly to the solution pair with $(\beta, m) = (1, 0)$, the trajectory of the solution

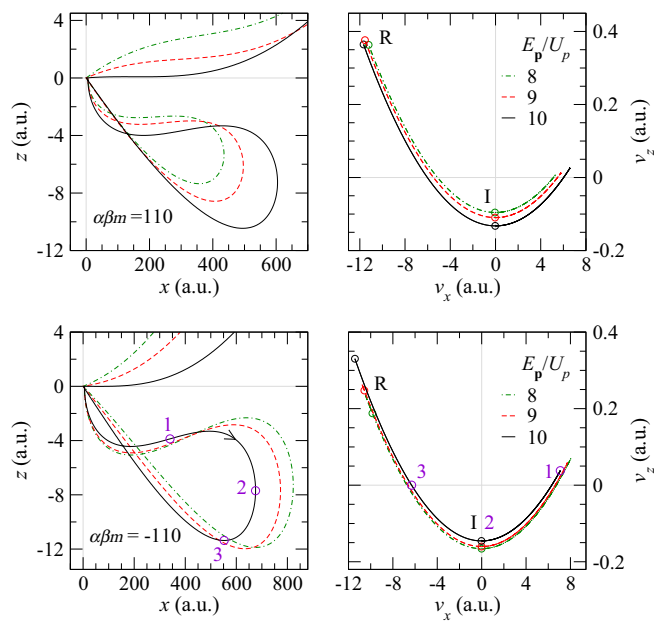


FIG. 2. Photoelectron trajectories (left panels) and corresponding velocities (right panels) for the SP solutions $(\alpha, \beta, m) = (1, 1, 0)$ (upper panels) and $(\alpha, \beta, m) = (-1, 1, 0)$ (lower panels) for photoelectron energies $8U_p, 9U_p,$ and $10U_p$. The ionization (rescattering) velocities are indicated by the letter I (R). For the solution $(\alpha, \beta, m) = (-1, 1, 0)$ and the photoelectron energy $10U_p$ we marked the intermediate steps in the electron’s trajectory and velocity by the violet circles.

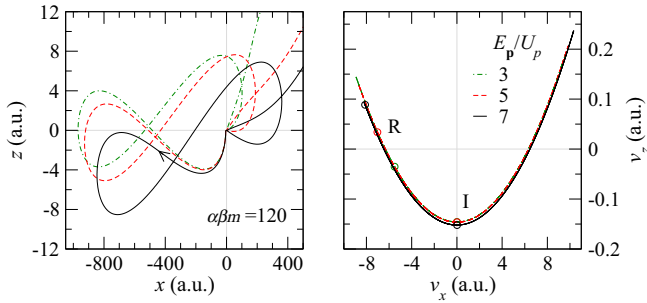


FIG. 3. Photoelectron trajectories (left panel) and corresponding velocities (right panel) for the SP solution $(\alpha, \beta, m) = (1, 2, 0)$ for photoelectron energies $3U_p$, $5U_p$, and $7U_p$, presented in a similar manner as in Fig. 2.

$(\alpha, \beta, m) = (-1, 2, 0)$ (not shown in Fig. 3) has the same shape as the trajectory of the solution $(\alpha, \beta, m) = (1, 2, 0)$, but with a slightly longer orbit because of its longer travel time. In addition, for the solution $(\alpha, \beta, m) = (1, 2, 0)$ the orbits slowly get longer as we get closer to the cutoff energy. Similarly to the solution pair $(\beta, m) = (1, 0)$, the orbit starts near the origin, with $v_x \approx 0$ and $v_z < 0$. However, the electron now moves in $x < 0$, as well as in $x \geq 0$, part of the xz plane. This can be explained by the fact that, for this solution, the electron spends more than one laser-field period in the laser field before the rescattering, and therefore the electric field changes its direction twice. At the beginning, the electron moves in the negative x direction, and after the electric field changes its sign for the first time it starts to accelerate toward the origin. However, this time, the electron misses the parent ion and goes into the positive part $x > 0$ of the xz plane. After the electric field changes direction for the second time, the electron starts to decelerate and eventually goes back to the origin where it rescatters of the parent ion.

The trajectories which correspond to different saddle-point solutions exhibit different behavior in the xz plane and the shape of the trajectory also depends quantitatively on the photoelectron energy. Now we investigate the influence of the nondipole effects on the partial contributions of the saddle-point solutions to the differential ionization rate. The question is whether all partial contributions are affected in the same way and how the influence of the nondipole effects changes the partial contributions for different values of the photoelectron energy. To quantify the influence of the nondipole corrections, we introduce the normalized difference $\delta_{pi} = (w_{pi}^{nd} - w_{pi}^{dip}) / (w_{pi}^{nd} + w_{pi}^{dip})$ between the differential ionization rates calculated using nondipole corrections (“nd”) and in the framework of the dipole approximation (“dip”). In Fig. 4 we present the normalized difference δ_{pi} as a function of the photoelectron energy for the partial contributions of the SP solutions, as indicated in the legend, and for the same driving-field parameters as in Fig. 1. Clearly, the influence of the nondipole effects is different for the contributions of different saddle-point solutions both qualitatively and quantitatively. For some solutions, such as $(\beta, m) = (2, 0)$ (green solid and dashed lines), $(\alpha, \beta, m) = (1, 1, 1)$ (blue solid line), and $(\alpha, \beta, m) = (-1, 1, 0)$ (red solid line), the parameter δ_{pi} has a negative value which is relatively constant for the

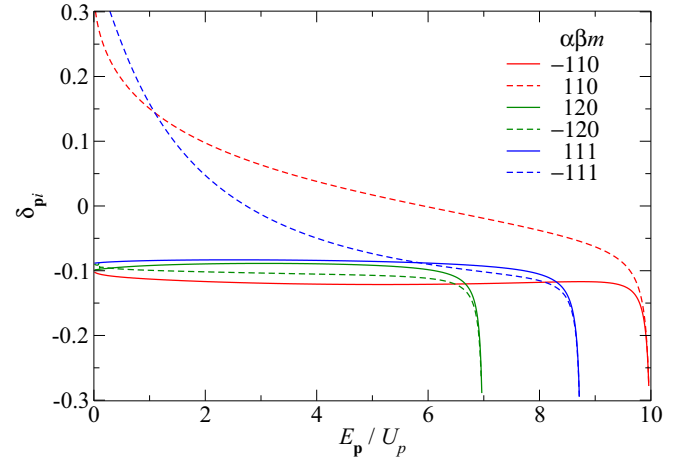


FIG. 4. Normalized difference δ_{pi} as a function of the photoelectron energy for the partial contributions of the SP solutions, as indicated in the legend. The driving-field parameters are the same as in Fig. 1.

photoelectron energy lower than the cutoff energy. For these solutions, the differential ionization rate is decreased due to the nondipole effects. On the other hand, for the solutions $(\alpha, \beta, m) = (1, 1, 0)$ (red dashed line) and $(\alpha, \beta, m) = (-1, 1, 1)$ (blue dashed line), the parameter δ_{pi} goes from the positive to the negative value with the increase of the photoelectron energy. This means that the nondipole effects deform the spectrum which corresponds to these solutions in such a way that they shift the spectrum up or down depending on the value of the photoelectron energy. The reason why the partial contributions are not affected equally by the nondipole effects lays in the fact that these solutions have different ionization and rescattering time so that they are under the influence of the magnetic field which is not the same for all contributions. This leads to the suppression of some and promotion of other quantum pathways. Similar behavior may also be present for partial contributions which correspond to the longer SP times (not shown in the figure) and for other values of the driving-field parameters. In other words, the nondipole corrections not only shift the photoelectron momentum distribution in the laser-field propagation direction, but also quantitatively change the differential ionization rate. This change is different for contributions of different saddle-point solutions.

B. Orthogonally polarized two-color field

After analyzing nondipole corrections for HATI induced by linearly polarized field we now turn our attention to the case of an OTC driving field. In particular, we investigate the $\omega-2\omega$ OTC field.

1. Direct electrons

First, we discuss the nondipole corrections for the direct electrons. In Fig. 5 we present the logarithm of the differential ionization rate for the He atom exposed to the $\omega-2\omega$ OTC field with component intensities $I = E_1^2 = E_2^2 = 5 \times 10^{14}$ W/cm², the fundamental wavelength of 2500 nm, and the relative phase (a) $\varphi = 0^\circ$, (b) $\varphi = 15^\circ$, and (c) $\varphi = 30^\circ$. The

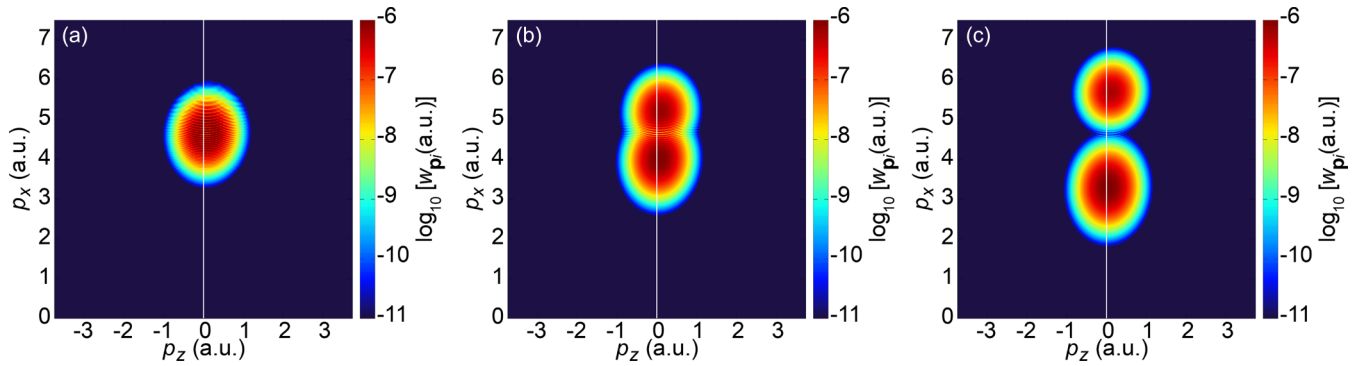


FIG. 5. Photoelectron momentum distribution for ATI induced by exposing the He atom to the ω - 2ω OTC field with component intensities $I = E_1^2 = E_2^2 = 5 \times 10^{14}$ W/cm², the fundamental wavelength of 2500 nm, and the relative phase (a) $\varphi = 0^\circ$, (b) $\varphi = 15^\circ$, and (c) $\varphi = 30^\circ$. The results are obtained using the theory which includes the nondipole corrections and calculated by the numerical integration. The white line is parallel to the p_x axis and goes through the origin. Only the results in the $p_x > 0$ part of the momentum plane are presented.

momentum distributions were obtained by numerical integration taking into account the nondipole effects. For the ω - 2ω OTC field, the photoelectron momentum distribution is invariant with respect to the reflection $p_x \rightarrow -p_x$ so that we only presented the results in the $p_x > 0$ part of the momentum plane. Due to the nondipole corrections, the reflection symmetry $p_z \rightarrow -p_z$ is broken. The effects of the nondipole corrections are subtle so that we included the white line as an aid to guide the eye. The nondipole corrections slightly distort the distributions and shift them in the positive p_z direction. This shift becomes more significant as the photoelectron energy increases. The shift of the momentum distribution in the propagation direction appears due to the momentum transfer to the photoelectrons. The p_z component of the photoelectron momentum is proportional to the energy of the absorbed photons from the laser field so that the shift becomes more pronounced as the photoelectron energy increases.

Before we analyze the nondipole corrections in more detail, let us discuss the dependence of the momentum distribution in the $p_z p_x$ plane on the value of the relative phase φ . For $\varphi = 0^\circ$ [see Fig. 5(a)], the momentum distribution is localized in the narrow region of the momentum plane and exhibits an oscillatory character as a function of the photoelectron energy. As the value of the relative phase increases, the two regions with significant differential ionization rates appear. In these regions, the photoelectron momentum distribution is smooth. This behavior can be explained using the SP method. For the ω - 2ω OTC driving field, the direct SP equation has $2s = 4$ solutions [81]. In Fig. 6 we present the logarithm of the differential ionization rate as a function of the photoelectron energy (black solid lines) calculated using the SP method with nondipole corrections for the emission in the direction $\phi = 0^\circ$, $\theta = 87^\circ$. The emission is induced by the ω - 2ω OTC field with the relative phase as indicated above the panels and for the same other field parameters as in Fig. 5. Besides the total spectrum, the partial contributions of different SP solutions are also presented (red solid and blue dashed lines). For the used values of the driving-field parameters, the contributions of two SP solutions $\eta = 2, 3$ are significant, while the contributions of the solutions $\eta = 1, 4$ are negligible. For the driving field with the relative phase

$\varphi = 0^\circ$ the partial contributions of the solutions $\eta = 2, 3$ are identical and their interference leads to the rapid oscillations of the spectrum [see also Fig. 5(a)]. As the relative phase φ increases, the partial contribution of the solution $\eta = 2$ ($\eta = 3$) moves towards the lower (higher) energy, and for the value $\varphi = 15^\circ$ they are comparable only in the narrow region around $0.8U_p$. Consequently, the rapid oscillations are present only in this part of the spectrum, while other parts are smooth [see also Fig. 5(b)]. To investigate what is happening with the partial contributions to the differential ionization rate for other values of the relative phase, in Fig. 7 we display the logarithm of the differential ionization rate as a function of the photoelectron energy E_p and the relative phase φ . For all values of the relative phase and for all values of the photoelectron energy, the partial contributions of the solutions $\eta = 1, 4$ are negligible, while the solutions $\eta = 2$ and $\eta = 3$ contribute for the energy $E_p < 0.8U_p$ and $E_p > 0.8U_p$, respectively. The exception happens for the relative phase around $\varphi = 0^\circ$ modulo π in which case the partial contributions of the solutions

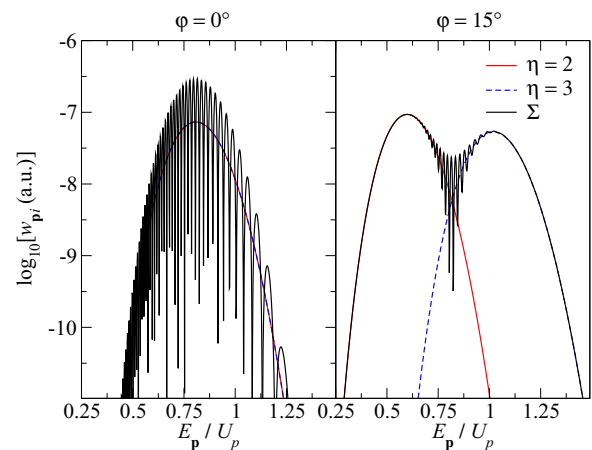


FIG. 6. Photoelectron spectrum (black solid lines) induced by the ω - 2ω OTC field with the relative phase as indicated above the panels and for the same other field parameters as in Fig. 5 together with the partial contributions of different SP solutions (red solid and blue dashed lines). The emission direction is $\phi = 0^\circ$, $\theta = 87^\circ$. Only direct electrons are taken into consideration.

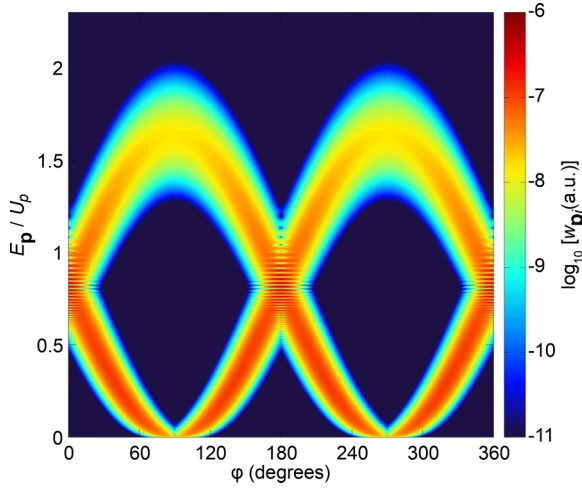


FIG. 7. Logarithm of the differential ionization rate as a function of the photoelectron energy E_p and the relative phase φ for ATI induced by the same driving field as in Fig. 5.

$\eta = 2, 3$ are comparable (for $\varphi = 0^\circ$ modulo π , they are the same) thus leading to the rapid oscillations of the spectrum.

The partial average value of the momentum p_z as a function of p_x ,

$$\langle p_z \rangle_{p_x} = \frac{\int dp_z p_z w_{pi}}{\int dp_z w_{pi}}, \quad (23)$$

can serve as a quantitative measure of the importance of the nondipole effects. In the dipole approximation it is $\langle p_z \rangle_{p_x} = 0$ and the spectrum possesses the $p_z \rightarrow -p_z$ reflection symmetry. The parameter $\langle p_z \rangle_{p_x}$ was used in Refs. [14,15] to discuss the negative offset along the propagation direction of the momentum distributions in the low-energy region which was related to a Coulomb focusing effects. However, in Refs. [39,41] a similar offset was reported for the negative molecular ions where the Coulomb interaction is absent. Instead, the offset was related to the oscillations caused by the interference of the contributions of different SP solutions. In Fig. 8 we present the partial average value $\langle p_z \rangle_{p_x}$ for the

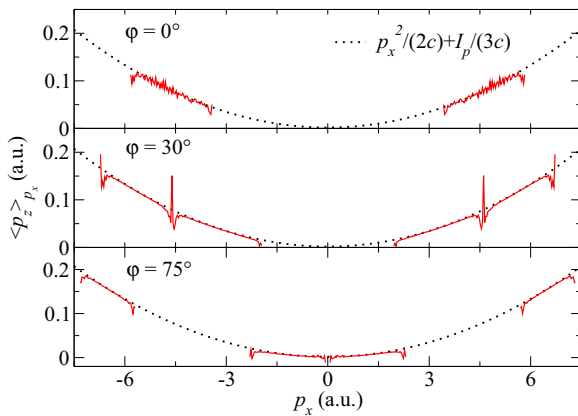


FIG. 8. The partial average value $\langle p_z \rangle_{p_x}$ (red solid line) for the coherent sum of the SP solutions $\eta = 2, 3$ and for the values of the relative phase as indicated in the panels. Other driving-field parameters are the same as in Fig. 5. The semiclassical estimate is presented by the black dotted lines.

coherent sum of the SP solutions $\eta = 2, 3$ and for the values of the relative phase as indicated in the panels. Other field parameters are the same as in Fig. 5. The partial average is presented only for those parts of the photoelectron spectrum in which the differential ionization rate is non-negligible. The momentum transfers to the photoelectron and the parent ion happen in such a way that the amount of the momentum which goes to the photoelectron is $I_p/(3c)$ so that the semiclassical approximation for the partial average leads to $p_x^2/(2c) + I_p/(3c)$ [16,19,84–89]. This approximation is represented via the black dotted line in Fig. 8. For the driving field with the relative phase $\varphi = 0^\circ$ both SP solutions $\eta = 2, 3$ contribute to the spectrum for the same range of values of the photoelectron energy. This causes the oscillations in the partial average $\langle p_z \rangle_{p_x}$. However, for our driving field with $\varphi = 0^\circ$, both partial contributions to the differential ionization rate are small for p_x close to zero so that the offset in the direction opposite to the propagation direction cannot be observed. In principle, there is not much point to calculate the partial average value $\langle p_z \rangle_{p_x}$ in the region where the ATI yield is negligible. Similar conclusions hold for other values of the relative phase. Particularly interesting is the region $65^\circ < \varphi < 115^\circ$ for which one SP solution gives a significant contribution around the origin in the momentum plane. For example, for $\varphi = 75^\circ$ (see the bottom panel in Fig. 8) the solution $\eta = 2$ leads to the significant contribution to the differential ionization rate for $-2.5 \text{ a.u.} < p_z < 2.5 \text{ a.u.}$ However, because this is the only solution which contributes significantly in this region of p_x , the partial average $\langle p_z \rangle_{p_x}$ is a smooth function and the offset in the direction opposite to the propagation direction is absent.

Finally, we mention that another way to quantitatively investigate the influence of the nondipole effects on the photoelectron momentum distribution is by presenting the one-dimensional slices through the two-dimensional momentum distribution. To accurately investigate the nondipole effects using this parameter, it is necessary to use the average values of the differential ionization rate (over some interval of the momentum p_x) to suppress the rapid oscillations [14].

2. Rescattered electrons

After analyzing direct electrons, we now turn our attention to the rescattered electrons. In Fig. 9 we present the photoelectron spectrum for HATI induced by exposing the He atom to the $\omega-2\omega$ OTC field with the fundamental wavelength 1500 nm, the relative phase $\varphi = 90^\circ$, and the same other parameters as in Fig. 5, calculated using the SP method (indigo solid line, circles) and by the numerical integration (orange solid line, circles), for the emission in the direction $\phi = 0^\circ, \theta = 87^\circ$. The partial contributions to the differential ionization rate which correspond to different saddle-point solutions and which are non-negligible are also presented as indicated in the legend. The agreement between the results calculated using the SP method (orange solid lines, circles) and the numerical integration (violet solid line, circles) is good, but still not as good as for a linearly polarized field [cf. Fig. 1(b) with Fig. 9]. This happens because, for the $\omega-2\omega$ OTC field there are many more solutions than for the monochromatic linearly polarized field. These solutions, may affect interferences even though their partial contributions are

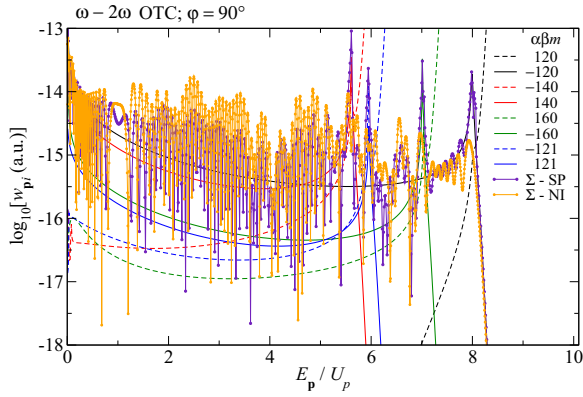


FIG. 9. Partial contributions to the differential ionization rate of different saddle-point solutions together with the coherent sum of these contributions (indigo solid line, circles) and the results obtained by the numerical integration (orange solid line, circles) for HATI induced by exposing the He atom to the ω - 2ω OTC field with the fundamental wavelength 1500 nm, the relative phase $\varphi = 90^\circ$ and other parameters as in Fig. 5. The electron emission direction is $\phi = 0^\circ$, $\theta = 87^\circ$. The results are obtained using the theory which includes the nondipole corrections and only rescattered electrons are taken into consideration.

small. This becomes more pronounced for the driving field with rich dynamics. For the photoelectron energy $E_p > 6U_p$, the spectrum is dominantly determined by the saddle-point solution $(\alpha, \beta, m) = (-1, 2, 0)$ (see the black solid line in Fig. 9) except in the region around $7U_p$ where the contribution of the solutions with $(\beta, m) = (6, 0)$ should also be taken into consideration. On the other hand, for $E_p < 6U_p$, apart from the $(\alpha, \beta, m) = (-1, 2, 0)$ solution, the solution $(\alpha, \beta, m) = (1, 4, 0)$ also contributes significantly to the HATI yield. The interplay of the contributions of these solutions creates the oscillatory pattern in the total spectrum. The nondipole effects for the photoelectron yield obtained by the OTC field can be analyzed in the same way as it was done for the bicircular field in Ref. [41]. However, in the present paper we devote particular attention to the influence of the nondipole corrections on the photoelectron trajectories. This is why, in this part of the paper, we have used the driving field with the fundamental wavelength 1500 nm instead of the earlier one with the fundamental wavelength of 2500 nm. For the fundamental wavelength much longer than 1500 nm, only one saddle-point solution accurately determines the high-energy part of the spectrum [usually the one with $(\beta, m) = (2, 0)$] and the examination of the influence of the nondipole corrections only makes sense for this solution. For the wavelength around 1500 nm, the nondipole corrections are still significant while more than one trajectories have to be taken into consideration to reproduce the spectra.

In Fig. 10 we present the quantum orbits (left panels) and corresponding velocities (right panels) for the above-mentioned solutions $(\alpha, \beta, m) = (-1, 2, 0)$ (black solid lines) and $(\alpha, \beta, m) = (1, 4, 0)$ (red dashed lines) and for the photoelectron energies $7U_p$ and $5U_p$. In addition to that, in Fig. 11 we present the electric field $\mathbf{E}(t)$, vector potential $\mathbf{A}(t)$, and magnetic field $\mathbf{B}(t)$ (blue solid lines), as well as their values at the moments of ionization (circles) and rescattering

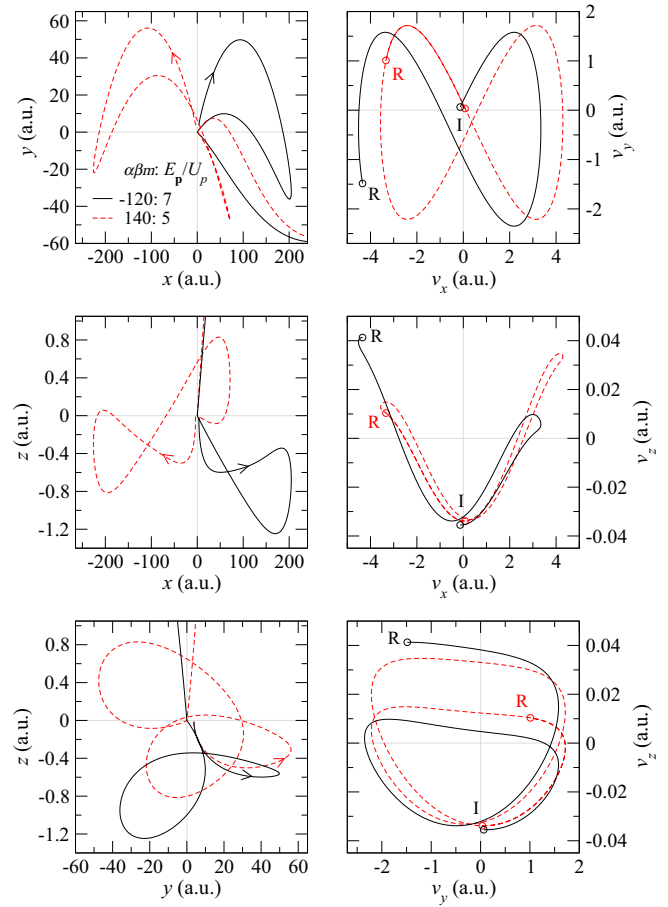


FIG. 10. The xy , xz , and yz projections of the electron trajectories (left panels) and velocities (right panels) in the OTC laser field for the SP solutions $(\alpha, \beta, m) = (-1, 2, 0)$ (black solid lines) and $(\alpha, \beta, m) = (1, 4, 0)$ (red dashed lines) for the electron energies $7U_p$ and $5U_p$, respectively. The velocities at the moment of ionization (rescattering) are indicated by the letter I (R).

(stars) for the two mentioned solutions. The ionization takes place at the moment when the electric field approximately reaches its maximal value, while rescattering takes place when vector potential is near its maximal value. Furthermore, the moments when both the electric field and the magnetic field are maximal coincide [see Eq. (13)], so that the ionization

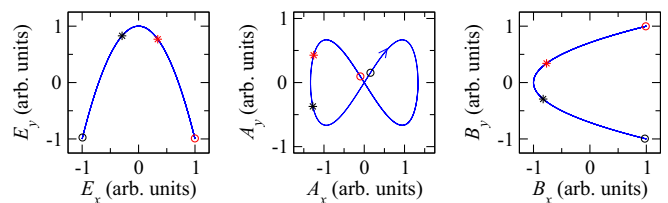


FIG. 11. Electric-field vector $\mathbf{E}(t)$, vector potential $\mathbf{A}(t)$, and magnetic-field vector $\mathbf{B}(t)$ (from left to right) for the OTC field with equal intensities of two components and relative phase $\varphi = 90^\circ$. Black (red) circles and stars denote the values of mentioned vectors at the moments of ionization and rescattering, respectively, for the SP solution $(\alpha, \beta, m) = (-1, 2, 0)$ [$(\alpha, \beta, m) = (1, 4, 0)$] and electron energy $7U_p$ ($5U_p$).

takes place at the moment when the magnetic field is also approximately maximal, explaining the abrupt change in the z coordinate right after the ionization (see the middle left panel of Fig. 10). The xy projections of the electron trajectories have a shape similar to that of the electric field because these are not affected by the nondipole effects. The projection of the electron velocity on the $v_x v_y$ plane is also not affected by the nondipole corrections and this projection has nearly the same shape as the vector potential (cf. the upper right panel of Fig. 10 with the middle panel of Fig. 11) [90]. On the other hand, the projections of the photoelectron trajectories and velocities onto the xz and yz , and onto the $v_x v_z$ and $v_y v_z$ planes are influenced by the nondipole effects. The photoelectron trajectories are now three dimensional. For example, the xz projection of the trajectory (and velocity) which corresponds to the solution $(\alpha, \beta, m) = (-1, 2, 0)$ for the $\omega-2\omega$ OTC driving field (see the black solid line in the middle-left panel of Fig. 10) is similar in shape to the solution $(\alpha, \beta, m) = (-1, 1, 0)$ for the linearly polarized driving field (see Fig. 2). This happens because the OTC field consists of two linearly polarized fields with mutually orthogonal polarizations, one with the polarization in the x and one with the polarization in the y direction. The electron motion along the x axis or the y axis is governed only by the driving field with the polarization along these directions. Moreover, the $\omega-2\omega$ OTC SP solution $(\alpha, \beta, m) = (-1, 2, 0)$ and the linearly polarized field solution $(\alpha, \beta, m) = (-1, 1, 0)$ have similar travel times. In addition, the quantum orbit of the solution $(\alpha, \beta, m) = (-1, 2, 0)$ for the $\omega-2\omega$ OTC driving field is much more elongated in the x -axis direction than in the y -axis direction, so that the term $v_x(t)E_x(t)/c$ dominates in comparison with the term $v_y(t)E_y(t)/c$ in Eq. (16). Similar conclusions hold if we compare the $(\alpha, \beta, m) = (1, 4, 0)$ solution for the $\omega-2\omega$ OTC driving field (see the black solid line in the lower-left panel of Fig. 10) and $(\alpha, \beta, m) = (1, 2, 0)$ solution for the linearly polarized field (see Fig. 2). Finally, the yz projections of the trajectories and velocities are directly obtained by combining the corresponding xy and xz projections. These trajectories are strongly affected not just by the field components, but also by the shape of the entire field.

In the end, we remark that the presented results are obtained using the long pulse with a flat envelope. The use of the ultrashort pulses with one or two carrier frequencies may alter the derived conclusions due to the dependence of the observables on the pulse length and the type of the pulse envelope.

IV. CONCLUSIONS

Recently, the laser facilities which generate mid-infrared radiation with high intensity have become readily available. In this case, the use of the dipole approximation to investigate the strong-field processes becomes questionable. The alternative approach assumes that a fully relativistic theory is employed to model the process and calculate the observable quantities. The corrections introduced by this theory are of the order of $1/c^2$, where c is the speed of light. However, for the driving fields with parameters which are just beyond the region in which the dipole approximation can be used, the relativistic

treatment is still not necessary, and the nondipole corrections, which are of the order of $1/c$, can be introduced.

In the first part of the present paper, we investigated the nondipole corrections for the linearly polarized monochromatic field. The influence of these corrections on the photoelectron momentum spectra was analyzed in our previous publications. In the present paper, we employed the saddle-point method and the quantum-orbit theory to investigate how the electron motion in the laser field is affected by the nondipole effects. In particular, we found the saddle-point solutions which lead to significant contributions to the differential ionization rate and which have to be used to accurately reproduce the photoelectron spectrum. Then we analyzed the quantum orbits which correspond to these solutions. In particular, we analyzed the temporal evolution of the trajectories and velocities of the emitted photoelectrons. When the nondipole effects are taken into consideration, the electron trajectories, which are defined as the projections of the corresponding quantum orbit on the real plane, are two dimensional. We showed that the influence of the nondipole effects is different for different saddle-point solutions. The solutions which spend a longer time in the continuum have richer dynamics in the laser field before the rescattering event. The motion of the electron in the laser-field propagation direction may become significant. Finally, we analyzed the influence of the nondipole corrections on the partial contributions to the differential ionization rate which are related to different saddle-point solutions and we found that this influence is different for different partial contributions. The nondipole effects, to a certain extent, promote some and suppress other quantum pathways.

In the second part of our paper, we investigated the nondipole corrections for the strong-field ionization induced by the tailored laser field exemplified by the $\omega-2\omega$ orthogonally polarized two-color field. Interestingly, the studies of the nondipole effects for the tailored driving laser fields are rare. First, we analyzed the direct photoelectrons. For these electrons, we investigate the shift of the momentum distribution induced by the nondipole effects using the partial average value of the electron-momentum component in the propagation direction. The photoelectron spectrum depends to a significant extent on the relative phase so that the nondipole correction has to be considered as a function of this parameter. We have shown that the partial average value of the electron-momentum component in the propagation direction may exhibit either smooth character when only one saddle-point solution is significant, or it may exhibit rapid oscillations when two or more solutions have to be taken into consideration. For our $\omega-2\omega$ driving field, the low-energy shift in the propagation direction was not present. On the other hand, for the rescattered electrons, which spend much longer time under the influence of the driving field, we analyzed how the corresponding trajectories are affected by the nondipole corrections. For the two-component driving fields, the photoelectron trajectories are three dimensional. For our OTC driving field, the electron motion in the zx plane is governed mostly by the component which is linearly polarized in the x direction and by the nondipole corrections. Consequently, the photoelectron trajectory resembles the trajectory of electrons

liberated by a linearly polarized field having a similar travel time.

Considering that the bichromatic midinfrared-wavelength lasers with high intensity are already widely used to induce the strong-field processes [91,92], we believe that the analysis of the nondipole effects is crucial for simulations of these processes and accurate calculations of the observable quantities.

ACKNOWLEDGMENTS

We gratefully acknowledge support by the Ministry for Science, Higher Education and Youth, Canton Sarajevo, Bosnia and Herzegovina. D.H. would like to thank the University College London for its kind hospitality. This work was partly funded by Grant No. EP/T517793/1 from the UK Engineering and Physical Sciences Research Council.

-
- [1] C. I. Moore, J. P. Knauer, and D. D. Meyerhofer, Observation of the transition from Thomson to Compton scattering in multi-photon interactions with low-energy electrons, *Phys. Rev. Lett.* **74**, 2439 (1995).
- [2] D. D. Meyerhofer, J. P. Knauer, S. J. McNaught, and C. I. Moore, Observation of relativistic mass shift effects during high-intensity laser–electron interactions, *J. Opt. Soc. Am. B* **13**, 113 (1996).
- [3] H. R. Reiss, Limits on tunneling theories of strong-field ionization, *Phys. Rev. Lett.* **101**, 043002 (2008); **101**, 159901(E) (2008).
- [4] A. Ludwig, J. Maurer, B. W. Mayer, C. R. Phillips, L. Gallmann, and U. Keller, Breakdown of the dipole approximation in strong-field ionization, *Phys. Rev. Lett.* **113**, 243001 (2014).
- [5] H. R. Reiss, The tunnelling model of laser-induced ionization and its failure at low frequencies, *J. Phys. B: At., Mol. Opt. Phys.* **47**, 204006 (2014).
- [6] B. Willenberg, J. Maurer, B. W. Mayer, and U. Keller, Sub-cycle time resolution of multi-photon momentum transfer in strong-field ionization, *Nat. Commun.* **10**, 5548 (2019).
- [7] C. T. L. Smeenk, L. Arissian, B. Zhou, A. Mysyrowicz, D. M. Villeneuve, A. Staudte, and P. B. Corkum, Partitioning of the linear photon momentum in multiphoton ionization, *Phys. Rev. Lett.* **106**, 193002 (2011).
- [8] N. Haram, I. Ivanov, H. Xu, K. T. Kim, A. Atia-tul Noor, U. S. Sainadh, R. D. Glover, D. Chetty, I. V. Litvinyuk, and R. T. Sang, Relativistic nondipole effects in strong-field atomic ionization at moderate intensities, *Phys. Rev. Lett.* **123**, 093201 (2019).
- [9] A. Hartung, S. Eckart, S. Brennecke, J. Rist, D. Trabert, K. Fehre, M. Richter, H. Sann, S. Zeller, K. Henrichs, G. Kastirke, J. Hoehl, A. Kalinin, M. S. Schöffler, T. Jahnke, L. Ph. H. Schmidt, M. Lein, M. Kunitski, and R. Dörner, Magnetic fields alter strong-field ionization, *Nat. Phys.* **15**, 1222 (2019).
- [10] A. Hartung, S. Brennecke, K. Lin, D. Trabert, K. Fehre, J. Rist, M. S. Schöffler, T. Jahnke, L. Ph. H. Schmidt, M. Kunitski, M. Lein, R. Dörner, and S. Eckart, Electric nondipole effect in strong-field ionization, *Phys. Rev. Lett.* **126**, 053202 (2021).
- [11] M.-X. Wang, S.-G. Chen, H. Liang, and L.-Y. Peng, Review on non-dipole effects in ionization and harmonic generation of atoms and molecules, *Chin. Phys. B* **29**, 013302 (2020).
- [12] N. Haram, R. T. Sang, and I. V. Litvinyuk, Transverse electron momentum distributions in strong-field ionization: nondipole and Coulomb focusing effects, *J. Phys. B: At., Mol. Opt. Phys.* **53**, 154005 (2020).
- [13] J. Maurer and U. Keller, Ionization in intense laser fields beyond the electric dipole approximation: concepts, methods, achievements and future directions, *J. Phys. B: At., Mol. Opt. Phys.* **54**, 094001 (2021).
- [14] S. Brennecke and M. Lein, High-order above-threshold ionization beyond the electric dipole approximation, *J. Phys. B: At., Mol. Opt. Phys.* **51**, 094005 (2018).
- [15] S. Brennecke and M. Lein, High-order above-threshold ionization beyond the electric dipole approximation: Dependence on the atomic and molecular structure, *Phys. Rev. A* **98**, 063414 (2018).
- [16] H. Ni, S. Brennecke, X. Gao, P.-L. He, S. Donsa, I. Březinová, F. He, J. Wu, M. Lein, X.-M. Tong, and J. Burgdörfer, Theory of subcycle linear momentum transfer in strong-field tunneling ionization, *Phys. Rev. Lett.* **125**, 073202 (2020).
- [17] S. Brennecke and M. Lein, Nondipole modification of the ac Stark effect in above-threshold ionization, *Phys. Rev. A* **104**, L021104 (2021).
- [18] K. Lin, S. Brennecke, H. Ni, X. Chen, A. Hartung, D. Trabert, K. Fehre, J. Rist, X.-M. Tong, J. Burgdörfer *et al.*, Magnetic-field effect in high-order above-threshold ionization, *Phys. Rev. Lett.* **128**, 023201 (2022).
- [19] S. V. B. Jensen, M. M. Lund, and L. B. Madsen, Nondipole strong-field-approximation Hamiltonian, *Phys. Rev. A* **101**, 043408 (2020).
- [20] S. V. B. Jensen and L. B. Madsen, Nondipole effects in laser-assisted electron scattering, *J. Phys. B: At., Mol. Opt. Phys.* **53**, 195602 (2020).
- [21] M. M. Lund and L. B. Madsen, Nondipole photoelectron momentum shifts in strong-field ionization with mid-infrared laser pulses of long duration, *J. Phys. B: At., Mol. Opt. Phys.* **54**, 165602 (2021).
- [22] L. B. Madsen, Nondipole effects in tunneling ionization by intense laser pulses, *Phys. Rev. A* **105**, 043107 (2022).
- [23] S. V. B. Jensen and L. B. Madsen, Propagation time and nondipole contributions to intraband high-order harmonic generation, *Phys. Rev. A* **105**, L021101 (2022).
- [24] S. Fritzsche and B. Böning, Lorentz-force shifts in strong-field ionization with mid-infrared laser fields, *Phys. Rev. Res.* **4**, 033031 (2022).
- [25] D. B. Milošević, S. X. Hu, and W. Becker, Quantum-mechanical model for ultrahigh-order harmonic generation in the moderately relativistic regime, *Phys. Rev. A* **63**, 011403(R) (2000).
- [26] M. W. Walser, C. H. Keitel, A. Scrinzi, and T. Brabec, High harmonic generation beyond the electric dipole approximation, *Phys. Rev. Lett.* **85**, 5082 (2000).
- [27] D. B. Milošević, S. X. Hu, and W. Becker, Relativistic ultrahigh-order harmonic generation, *Laser Phys.* **12**, 389 (2002).

- [28] D. B. Milošević and W. Becker, Relativistic high-order harmonic generation, *J. Mod. Opt.* **50**, 375 (2003).
- [29] B. Minneker, B. Böning, and S. Fritzsche, Generalized nondipole strong-field approximation of high-order harmonic generation, *Phys. Rev. A* **106**, 053109 (2022).
- [30] F. C. Vélez, K. Krajewska, and J. Z. Kamiński, Generation of electron vortex states in ionization by intense and short laser pulses, *Phys. Rev. A* **97**, 043421 (2018).
- [31] M. C. Suster, J. Derlikiewicz, K. Krajewska, F. C. Vélez, and J. Z. Kamiński, Nondipole signatures in ionization and high-order harmonic generation, *Phys. Rev. A* **107**, 053112 (2023).
- [32] D. F. Dar, B. Minneker, and S. Fritzsche, Nondipole strong-field approximation for above-threshold ionization in a few-cycle pulse, *Phys. Rev. A* **107**, 053102 (2023).
- [33] M. Førre, Nondipole effects and photoelectron momentum shifts in strong-field ionization by infrared light, *Phys. Rev. A* **106**, 013104 (2022).
- [34] C. Figueira de Morisson Faria and A. S. Maxwell, It is all about phases: ultrafast holographic photoelectron imaging, *Rep. Prog. Phys.* **83**, 034401 (2020).
- [35] A. P. Woźniak, M. Przybytek, M. Lewenstein, and R. Moszyński, Effects of electronic correlation on the high harmonic generation in helium: A time-dependent configuration interaction singles vs time-dependent full configuration interaction study, *J. Chem. Phys.* **156**, 174106 (2022).
- [36] K. Finger, D. Atri-Schuller, N. Douguet, K. Bartschat, and K. R. Hamilton, High-order harmonic generation in the water window from mid-IR laser sources, *Phys. Rev. A* **106**, 063113 (2022).
- [37] D. B. Milošević and F. Ehlötzky, Scattering and reaction processes in powerful laser fields, *Adv. At. Mol. Opt. Phys.* **49**, 373 (2003).
- [38] T. Rook, D. Habibović, L. Cruz Rodríguez, D. B. Milošević, and C. Figueira de Morisson Faria, Impact of the continuum Coulomb interaction in quantum-orbit-based treatments of high-order above-threshold ionization, *Phys. Rev. A* **109**, 033115 (2024).
- [39] R. Kahvedžić and S. Gräfe, Strong-field approximation with leading-order nondipole corrections, *Phys. Rev. A* **105**, 063102 (2022).
- [40] D. Habibović and D. B. Milošević, Strong-field ionization of atoms beyond the dipole approximation, *Phys. Rev. A* **106**, 033101 (2022).
- [41] R. Kahvedžić, D. Habibović, W. Becker, S. Gräfe, and D. B. Milošević, Nondipole effects in atomic ionization induced by an intense counter-rotating bicircular laser field, *Ann. Phys. (Berlin, Ger.)* **535**, 2200616 (2023).
- [42] J.-H. Chen, M. Han, X.-R. Xiao, L.-Y. Peng, and Y. Liu, Atomic-orbital-dependent photoelectron momentum distributions for F^- ions by orthogonal two-color laser fields, *Phys. Rev. A* **98**, 033403 (2018).
- [43] M. Li, J.-W. Geng, M.-M. Liu, X. Zheng, L.-Y. Peng, Q. Gong, and Y. Liu, Spatial-temporal control of interferences of multiple tunneling photoelectron wave packets, *Phys. Rev. A* **92**, 013416 (2015).
- [44] J.-W. Geng, W.-H. Xiong, X.-R. Xiao, L.-Y. Peng, and Q. Gong, Nonadiabatic electron dynamics in orthogonal two-color laser fields with comparable intensities, *Phys. Rev. Lett.* **115**, 193001 (2015).
- [45] J. Henkel and M. Lein, Analysis of electron trajectories with two-color strong-field ionization, *Phys. Rev. A* **92**, 013422 (2015).
- [46] M. He, Y. Li, Y. Zhou, M. Li, and P. Lu, Temporal and spatial manipulation of the recolliding wave packet in strong-field photoelectron holography, *Phys. Rev. A* **93**, 033406 (2016).
- [47] N. Eicke and M. Lein, Extracting trajectory information from two-color strong-field ionization, *J. Mod. Opt.* **64**, 981 (2017).
- [48] Y. Li, Y. Zhou, M. He, M. Li, and P. Lu, Identifying backward-rescattering photoelectron hologram with orthogonal two-color laser fields, *Opt. Express* **24**, 23697 (2016).
- [49] X. Gong, C. Lin, F. He, Q. Song, K. Lin, Q. Ji, W. Zhang, J. Ma, P. Lu, Y. Liu, H. Zeng, W. Yang, and J. Wu, Energy-resolved ultrashort delays of photoelectron emission clocked by orthogonal two-color laser fields, *Phys. Rev. Lett.* **118**, 143203 (2017).
- [50] M. Han, P. Ge, Y. Shao, M.-M. Liu, Y. Deng, C. Wu, Q. Gong, and Y. Liu, Revealing the sub-barrier phase using a spatiotemporal interferometer with orthogonal two-color laser fields of comparable intensity, *Phys. Rev. Lett.* **119**, 073201 (2017).
- [51] X. Xie, T. Wang, S. G. Yu, X. Y. Lai, S. Roither, D. Kartashov, A. Baltuška, X. J. Liu, A. Staudte, and M. Kitzler, Disentangling intracycle interferences in photoelectron momentum distributions using orthogonal two-color laser fields, *Phys. Rev. Lett.* **119**, 243201 (2017).
- [52] J. Tan, Y. Zhou, M. He, Y. Chen, Q. Ke, J. Liang, X. Zhu, M. Li, and P. Lu, Determination of the ionization time using attosecond photoelectron interferometry, *Phys. Rev. Lett.* **121**, 253203 (2018).
- [53] J. Tan, Y. Zhou, M. He, Q. Ke, J. Liang, Y. Li, M. Li, and P. Lu, Time-resolving tunneling ionization via strong-field photoelectron holography, *Phys. Rev. A* **99**, 033402 (2019).
- [54] W. Xie, M. Li, S. Luo, M. He, K. Liu, Q. Zhang, Y. Zhou, and P. Lu, Nonadiabaticity-induced ionization time shift in strong-field tunneling ionization, *Phys. Rev. A* **100**, 023414 (2019).
- [55] M. Li, H. Xie, W. Cao, S. Luo, J. Tan, Y. Feng, B. Du, W. Zhang, Y. Li, Q. Zhang, P. Lan, Y. Zhou, and P. Lu, Photoelectron holographic interferometry to probe the longitudinal momentum offset at the tunnel exit, *Phys. Rev. Lett.* **122**, 183202 (2019).
- [56] M. Han, P. Ge, Y. Fang, Y. Deng, C. Wu, Q. Gong, and Y. Liu, Quantum effect of laser-induced rescattering from the tunneling barrier, *Phys. Rev. A* **99**, 023418 (2019).
- [57] F. Jin, H. Yang, B. Wang, L. Wei, and H. Wu, Angular resolved above-threshold ionization spectrum of an atom in IR + XUV orthogonally polarized two-color laser fields, *Opt. Express* **27**, 20754 (2019).
- [58] Y. Liu, J. Tan, M. He, H. Xie, Y. Qin, Y. Zhao, M. Li, Y. Zhou, and P. Lu, Photoelectron holographic interferences from multiple returning in strong-field tunneling ionization, *Opt. Quantum Electron.* **51**, 145 (2019).
- [59] F. Lindner, M. G. Schätzel, H. Walther, A. Baltuška, E. Goulielmakis, F. Krausz, D. B. Milošević, D. Bauer, W. Becker, and G. G. Paulus, Attosecond double-slit experiment, *Phys. Rev. Lett.* **95**, 040401 (2005).
- [60] M. Richter, M. Kunitski, M. Schöffler, T. Jahnke, L. P. H. Schmidt, M. Li, Y. Liu, and R. Dörner, Streaking temporal double-slit interference by an orthogonal two-color laser field, *Phys. Rev. Lett.* **114**, 143001 (2015).
- [61] D. B. Milošević, Possibility of introducing spin into attoscience with spin-polarized electrons produced by a bichromatic

- circularly polarized laser field, *Phys. Rev. A* **93**, 051402(R) (2016).
- [62] M. Han, P. Ge, M.-M. Liu, Q. Gong, and Y. Liu, Spatially and temporally controlling electron spin polarization in strong-field ionization using orthogonal two-color laser fields, *Phys. Rev. A* **99**, 023404 (2019).
- [63] D. B. Milošević and W. Becker, X-ray harmonic generation by orthogonally polarized two-color fields: Spectral shape and polarization, *Phys. Rev. A* **100**, 031401(R) (2019).
- [64] D. Habibović and D. B. Milošević, Ellipticity of high-order harmonics generated by aligned homonuclear diatomic molecules exposed to an orthogonal two-color laser field, *Photonics* **7**, 110 (2020).
- [65] D. Habibović, W. Becker, and D. B. Milošević, High-order harmonic generation by planar polyatomic molecules exposed to an orthogonally polarized two-color laser field, *J. Phys. B: At., Mol. Opt. Phys.* **54**, 134004 (2021).
- [66] D. Habibović, K. R. Hamilton, O. Neufeld, and L. Rego, The application of tailored fields for studying chirality and symmetry, [arXiv:2404.05923](https://arxiv.org/abs/2404.05923) [Nat. Rev. Phys. (to be published)].
- [67] P. Salières, B. Carré, L. Le Déroff, F. Grasbon, G. G. Paulus, H. Walther, R. Kopold, W. Becker, D. B. Milošević, A. Sanpera, and M. Lewenstein, Feynman's path-integral approach for intense-laser-atom interactions, *Science* **292**, 902 (2001).
- [68] D. B. Milošević, A. S. Jašarević, D. Habibović, E. Hasović, A. Čerkić, and W. Becker, Asymptotic methods applied to integrals occurring in strong-laser-field processes, *J. Phys. A Math. Theor.* (2024), doi:10.1088/1751-8121/ad7212.
- [69] F. H. M. Faisal, Multiple absorption of laser photons by atoms, *J. Phys. B: At. Mol. Phys.* **6**, L89 (1973).
- [70] H. R. Reiss, Effect of an intense electromagnetic field on a weakly bound system, *Phys. Rev. A* **22**, 1786 (1980).
- [71] M. Lewenstein, K. C. Kulander, K. J. Schafer, and P. H. Bucksbaum, Rings in above-threshold ionization: A quasiclassical analysis, *Phys. Rev. A* **51**, 1495 (1995).
- [72] A. Lohr, M. Kleber, R. Kopold, and W. Becker, Above-threshold ionization in the tunneling regime, *Phys. Rev. A* **55**, R4003 (1997).
- [73] N. J. Kylstra, R. M. Potvliege, and C. J. Joachain, Photon emission by ions interacting with short intense laser pulses: Beyond the dipole approximation, *J. Phys. B: At., Mol. Opt. Phys.* **34**, L55 (2001).
- [74] E. Clementi and C. Roetti, Roothaan-Hartree-Fock atomic wavefunctions: Basis functions and their coefficients for ground and certain excited states of neutral and ionized atoms, $Z \leq 54$, *At. Data Nucl. Data Tables* **14**, 177 (1974).
- [75] A. D. McLean and R. S. McLean, Roothaan-Hartree-Fock atomic wave functions Slater basis-set expansions for $Z = 55-92$, *At. Data Nucl. Data Tables* **26**, 197 (1981).
- [76] C. F. Bunge, J. A. Barrientos, and A. V. Bunge, Roothaan-Hartree-Fock ground-state atomic wave functions: Slater-type orbital expansions and expectation values for $Z = 2-54$, *At. Data Nucl. Data Tables* **53**, 113 (1993).
- [77] A. A. Radzig and B. M. Smirnov, *Reference Data on Atoms, Molecules and Ions* (Springer, Berlin, 1985).
- [78] G. F. Gribakin and M. Y. Kuchiev, Multiphoton detachment of electrons from negative ions, *Phys. Rev. A* **55**, 3760 (1997).
- [79] E. Hasović, M. Busuladžić, A. Gazibegović-Busuladžić, D. B. Milošević, and W. Becker, Simulation of above-threshold ionization experiments using the strong-field approximation, *Laser Phys.* **17**, 376 (2007).
- [80] D. B. Milošević and W. Becker, Improved strong-field approximation and quantum-orbit theory: Application to ionization by a bicircular laser field, *Phys. Rev. A* **93**, 063418 (2016).
- [81] A. S. Jašarević, E. Hasović, R. Kopold, W. Becker, and D. B. Milošević, Application of the saddle-point method to strong-laser-field ionization, *J. Phys. A: Math. Theor.* **53**, 125201 (2020).
- [82] D. B. Milošević and W. Becker, Role of long quantum orbits in high-order harmonic generation, *Phys. Rev. A* **66**, 063417 (2002).
- [83] D. B. Milošević, E. Hasović, M. Busuladžić, A. Gazibegović-Busuladžić, and W. Becker, Intensity-dependent enhancements in high-order above-threshold ionization, *Phys. Rev. A* **76**, 053410 (2007).
- [84] A. S. Titi and G. W. F. Drake, Quantum theory of longitudinal momentum transfer in above-threshold ionization, *Phys. Rev. A* **85**, 041404(R) (2012).
- [85] M. Klaiber, E. Yakaboylu, H. Bauke, K. Z. Hatsagortsyan, and C. H. Keitel, Under-the-barrier dynamics in laser-induced relativistic tunneling, *Phys. Rev. Lett.* **110**, 153004 (2013).
- [86] S. Chelkowski, A. D. Bandrauk, and P. B. Corkum, Photon momentum sharing between an electron and an ion in photoionization: from one-photon (photoelectric effect) to multiphoton absorption, *Phys. Rev. Lett.* **113**, 263005 (2014).
- [87] S. Chelkowski, A. D. Bandrauk, and P. B. Corkum, Photon-momentum transfer in multiphoton ionization and in time-resolved holography with photoelectrons, *Phys. Rev. A* **92**, 051401(R) (2015).
- [88] A. Hartung, F. Morales, M. Kunitski, K. Henrichs, A. Laucke, M. Richter, T. Jahnke, A. Kalinin, M. Schöffler, L. Ph. H. Schmidt, M. Ivanov, O. Smirnova, and R. Dörner, Electron spin polarization in strong-field ionization of xenon atoms, *Nat. Photonics* **10**, 526 (2016).
- [89] P.-L. He, D. Lao, and F. He, Strong field theories beyond dipole approximations in nonrelativistic regimes, *Phys. Rev. Lett.* **118**, 163203 (2017).
- [90] A. S. Jašarević, E. Hasović, and D. B. Milošević, Ionization by a strong orthogonal two-color laser field: a quantum-orbit-theory approach, *Eur. Phys. J. D* **76**, 240 (2022).
- [91] M. Yeung, S. Rykovanov, J. Bierbach, L. Li, E. Eckner, S. Kuschel, A. Woldegeorgis, C. Rödel, A. Sävert, G. G. Paulus, M. Coughlan, B. Dromey, and M. Zepf, *Nat. Photonics* **11**, 32 (2017).
- [92] P. Mulse, Applications of High Power Lasers, in *Hot Matter from High-Power Lasers* (Springer, Berlin, Heidelberg, 2020), p. 677.